

This is the accepted manuscript made available via CHORUS. The article has been published as:

Measurement of the $^{65}\text{Cu}(n,\gamma)$ cross section using the Detector for Advanced Neutron Capture Experiments at LANL

C. J. Prokop, A. Couture, S. Jones, S. Mosby, G. Rusev, J. Ullmann, and M. Krťčka

Phys. Rev. C **99**, 055809 — Published 20 May 2019

DOI: [10.1103/PhysRevC.99.055809](https://doi.org/10.1103/PhysRevC.99.055809)

Measurement of the $^{65}\text{Cu}(n,\gamma)$ cross section using DANCE

C. J. Prokop,* A. Couture, S. Jones, S. Mosby, G. Rusev, and J. Ullmann
 Los Alamos National Laboratory, Los Alamos, New Mexico, 87545, USA

M. Krtićka

Charles University, V Holesšovicčkách 2, CZ-180 00 Prague 8, Czech Republic

(Dated: May 1, 2019)

Improving our understanding of the origin of the elements in the observable universe as well as the nature of the environments responsible for their production has been of paramount importance to the nuclear physics community. More than half of the isotopes of these elements are created via neutron-capture processes, and thus accurate measurements of the salient underlying nuclear physics, such as neutron-capture cross sections, masses, and β -decay half lives are crucial. Of particular importance to the synthesis of isotopes in the mass range of $A \approx 60$ to $A \approx 90$, via the weak s-process, are the neutron-capture cross sections of $^{63,65}\text{Cu}$, where large discrepancies between measurements exist. Recent measurements have addressed these discrepancies for ^{63}Cu [1], but questions still remain for ^{65}Cu . In this manuscript we report a new measurement of the $^{65}\text{Cu}(n,\gamma)$ cross-section performed using the Detector for Advanced Neutron Capture Experiments located at the Los Alamos Neutron Science Center of Los Alamos National Laboratory. The MACS for $^{65}\text{Cu}(n,\gamma)$ at $kT = 30$ keV deduced from this work is $(37.0 \pm 0.3_{\text{stat.}} \pm 3.3_{\text{sys.}})$ mb. The impact on weak s-process nucleosynthesis of new Maxwellian-Averaged Cross Sections, calculated over the range of $kT = 5$ keV to 100 keV, for ^{65}Cu , combined with the updated MACS for ^{63}Cu [1] and ^{63}Ni [2], were investigated. Results of this investigation show an increase of predicted nucleosynthesis yields of elements of Zn to Zr by as much as 20 percent.

PACS numbers:

PACS numbers: 28.20.Np, 24.30.Gd, 27.50.+e, 26.20.Kn

I. INTRODUCTION

Improving our understanding of the origin of the elements in the observable universe is of paramount importance. Most of the isotopes of the elements heavier than iron are formed by either the slow (s-process) or rapid (r-process) neutron-capture processes. While both the timescales and nature of the host environments are different, they are both characterized by the successive capture of neutrons on seed nuclei.

The s-process occurs in more quiescent environments with lower temperatures and neutron densities with a path along the neutron-rich edge of the valley of β stability. It can be further subdivided into a weak and main component. The former is responsible for producing several nuclei with $A \approx 60$ to $A \approx 90$ and occurs during helium-core and carbon-shell burning of massive stars, fueled by the $^{13}\text{C}(\alpha,n)^{16}\text{O}$ and $^{22}\text{Ne}(\alpha,n)^{25}\text{Mg}$ reactions. The later is thought to occur in thermally-pulsing low-mass Asymptotic Giant Branch (AGB) stars and creates isotopes from the ^{56}Fe seed up to ^{209}Bi where the process terminates [3]. Figure 1 shows the s-process path in the vicinity of ^{65}Cu .

The relatively shorter timescales and lower neutron densities of the weak s-process increase the impact of the input nuclear physics such as neutron-capture cross sections and β -decay half lives. In particular the neutron-

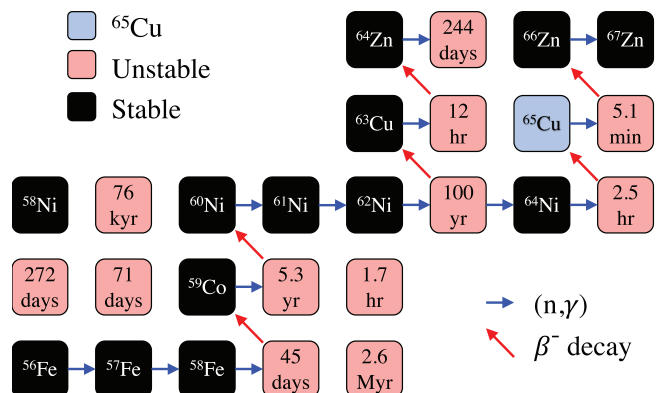


FIG. 1. (Color Online) Path of the s-process in the vicinity of ^{65}Cu . Isotopes shown in black are observationally stable, isotopes shown in salmon are unstable, and ^{65}Cu is highlighted in light blue. Blue arrows indicate neutron capture while red arrows indicate β^- decay.

capture cross sections of $^{63,65}\text{Cu}$ have both a large impact on the s-process abundances as well as significant discrepancies between existing measurements. Measurements made at ORELA in the 1970s on $^{63,65}\text{Cu}$ [4] yielded Maxwellian-Averaged Cross Sections (MACS) values of (94 ± 10) mb and (41 ± 5) mb at $kT = 30$ keV for ^{63}Cu and ^{65}Cu , respectively. A more recent activation measurement from Karlsruhe in 2008 [5] obtained MACS values of (56 ± 2.2) mb and (29.8 ± 1.3) mb at $kT = 30$ keV for ^{63}Cu and ^{65}Cu , respectively. The reduction of the

* cprokop@lanl.gov

$^{63,65}\text{Cu}$ neutron-capture cross sections reduced the nucleosynthesis yields of several isotopes between $A \approx 60$ and $A \approx 90$ at the 20% level.

Recently the ^{63}Cu neutron-capture cross section was remeasured [1] in a campaign via activation at the Joint Research Center (JRC) in Geel as well as by time-of-flight (TOF) at the Los Alamos Neutron Science Center (LANSCE) at Los Alamos National Laboratory (LANL) using the Detector for Advanced Neutron Capture Experiments (DANCE) [6]. This most recent $^{63}\text{Cu}(n,\gamma)$ measurement obtained a MACS value, of $(84.0 \pm 1.1_{\text{stat.}} \pm 6.7_{\text{sys.}})$ mb at $kT = 30$ keV. While this value is slightly lower than what was obtained from the work of Ref. [4], it is much higher than the activation measurements reported in Ref. [5]. The source of this discrepancy was determined to be primarily the influence of a 1-mm thick natural Cu backing material not accounted for in the cross section measurements from Ref. [5]. The natural Cu backing absorbed neutrons and reduced the number of activated ^{63}Cu nuclei, and thus the deduced $^{63}\text{Cu}(n,\gamma)$ cross section. Moreover, since ^{65}Cu is also stable, with a $\approx 30\%$ natural abundance, it is likely that a similar systematic error is also present for the $^{65}\text{Cu}(n,\gamma)$ cross section reported by Ref. [5]. The manuscript presented herein describes a new measurement of the $^{65}\text{Cu}(n,\gamma)$ cross section performed using DANCE at LANL to address these discrepancies.

II. EXPERIMENT

A. Experimental Setup

DANCE is positioned on flight path 14 of the Lujan Neutron Scattering Center at LANSCE [7] at a flight path length of 20.28 meters. Neutrons are produced via spallation of an 800-MeV proton beam, operating at a 20-Hz repetition rate, impinging onto a pair of tungsten targets, and subsequently moderated by a room-temperature backscatter water moderator [8]. The resulting epithermal neutron beam ranges in energy from a few meV to a few MeV and is collimated to a 7-mm diameter beam spot at the sample location.

DANCE [6] is a 160 element close-packed BaF_2 γ -ray calorimeter with a solid angle coverage of nearly 4π . Further downstream of DANCE exists a suite of three beam monitors which utilize the $^6\text{Li}(n,t)\alpha$, $^{235}\text{U}(n,f)$, and $^3\text{He}(n,p)$ reactions to detect neutrons. The measured yield from each beam monitor is directly proportional to the number of neutrons at the sample position.

DANCE and its associated beam monitors are read out using 16-channel CAEN VX1730 digitizers employing 14-bit 500-mega-sample-per-second digitizers. Each digitizer is synchronized with a common clock propagated sequentially from board to board [9]. All DANCE crystals and beam monitors trigger independently, however the DANCE crystals are validated by a timing gate of fixed width starting $\approx 100 \mu\text{s}$ before the arrival of the

protons on the tungsten target. The width of this gate, typically a few milliseconds, determines the range of neutron energies recorded by the acquisition system. Data is collected continuously until a specified file size, 4 GB for the present data, is reached at which point the run is stopped, the digitizers are reset and reprogrammed, and a new run is started. Nominal run lengths are 10 to 15 minutes.

A variety of information is recorded from DANCE and its associated beam monitors. In addition to the board and channel numbers, the leading-edge timestamp, long and short charge integrals, and partial waveforms are recorded for all channels. For each partial waveform a more precise fractional timestamp is determined offline from the location in time at which the rising edge of the detector signal crosses a threshold set by the last few samples of the partial waveform. The energy of each DANCE crystal, E_{Cr} , is calculated from the long integral minus the short integral to reduce the impact on linearity from overflowing of the fast component.

Based on the extracted timestamps for the DANCE crystals, a DANCE event is created by grouping all crystals identified as γ -rays via Pulse Shape Discrimination (PSD) that fired within a user-defined 5 ns coincidence window. The corresponding neutron energy, E_n , of the DANCE event is calculated from neutron TOF determined by the time difference between the first crystal of the DANCE event and the previous timing signal of the proton pulse immediately before it interacts with the tungsten spallation target. The sum of all γ ray energies in the DANCE event is recorded as E_{Sum} and the number of crystals participating in the event is denoted as M_{Cr} . Beam-monitor events are treated in a similar fashion, but without coincidence requirements as beam monitors are single, independent channels.

B. Samples

The primary sample for this experiment is a highly enriched (99.7%) ^{63}Cu cylinder, in metallic form, with a diameter of 4-mm and total mass of (219.2 ± 0.5) mg. Additional samples were also measured to assess backgrounds and contamination as well as normalize the neutron fluence. The ^{63}Cu sample used to characterize the $\approx 0.3\%$ ^{63}Cu contaminant was also in metallic form enriched to 99.88% ^{63}Cu . A 4-mm diameter 5-kÅ thick ^{197}Au sample and a ≈ 100 mg ^{208}Pb sample were also run for neutron fluence normalization and scattered-neutron background characterization, respectively.

C. Energy Calibrations

The BaF_2 crystals are temperature sensitive and have been observed to drift over time. Fortunately, the intrinsic internal activity from alpha decay of ^{226}Ra , a chemical homologue of Ba, inside the the BaF_2 crystals provides a

means for a run-by-run correction. The α -decay signals are distinguished from γ rays using PSD.

Before the start of data analysis an initial quadratic energy calibration was performed for each DANCE crystal using known lines from ^{22}Na , ^{88}Y , and PuBe sources as well as strong high-energy primary transitions from $^{59}\text{Co}(n, \gamma)$ measured immediately after the source runs. The combined α spectra of each crystal for the source runs, with the initial calibration applied, were saved as a template. In all subsequent, non-calibration, runs the uncalibrated α spectra were fit to these templates for each crystal to extract the energy calibration for that run. However, the limited energy range of the α spectra cannot adequately constrain the quadratic fit parameters so the linear and quadratic constants were fixed to their initial values, constraining the shape of the calibration, and then scaled by a single parameter left free along with the offset parameter.

D. Time Offsets and Flight Path Corrections

The relative timing of all crystals changes slightly for each run due to the synchronization of the digitizers. All crystals were aligned with one another in time on a run-by-run basis by adjusting their time offsets such that the difference between Compton scatter events in adjacent crystals was zero for each pair of crystals.

The complicated moderation process of neutrons in the spallation target-moderator assembly introduces a moderation time (ΔTOF) for neutrons, which is E_n dependent, that must be accounted for in the analysis. The measured time-of-flight ($\text{TOF}_{\text{Measured}}$) is the sum of the actual time of flight ($\text{TOF}_{\text{Actual}}$) of the neutron and ΔTOF . The $\Delta\text{TOF}/\text{TOF}_{\text{Actual}}$, for a given flight path length, as a function of E_n leaving the face of the moderator was deduced from a simulation of the target-moderator assembly [10]. The results of this simulation were then used to correct $\text{TOF}_{\text{Measured}}$ to $\text{TOF}_{\text{Actual}}$ event-by-event.

The global time offset for DANCE and each beam monitor along with its precise flight path length was deduced. Each instrument displays strong absorption in the E_n spectrum at 337.3 eV, 5.906 keV, 34.765 keV, and 86.183 keV from ^{27}Al and ^{55}Mn in beamline and moderator structural components. Resonances at 4.89 eV and 60.1 eV in $^{197}\text{Au}(n, \gamma)$ for DANCE and at 1.143 eV and 2.035 eV in $^{235}\text{U}(n, f)$ for the ^{235}U monitor were also used. The global time offset and flight-path length were varied simultaneously and E_n was calculated for each combination and each resonance along with the residual sum of squares (RSS) for each combination. The combination with the smallest RSS was used as the optimum global time offset and flight path length. This procedure was carried out independently for DANCE and each beam monitor.

E. Scattered-Neutron Background Characterization

Neutrons incident on samples in DANCE have a probability of scattering. Scattered neutrons subsequently thermalize through interactions with components inside and nearby DANCE, and can capture on the Ba in the BaF_2 crystals creating γ -ray signatures that are similar to the neutron-capture signal from samples of interest. This scattered-neutron background was characterized using a ^{208}Pb sample. The low 3.94-MeV Q-value of $^{208}\text{Pb}(n, \gamma)$ coupled with a relatively low neutron-capture cross section and a relatively high neutron elastic-scattering cross section makes it the ideal sample for this purpose. Fortunately, ^{135}Ba has a high 9.108-MeV Q-Value, which gives a clear signature of scattered-neutron background above the Q-values of interest for all samples run during this experiment.

In some instances the background over an isolated resonance was characterized by selecting regions either side of the resonance instead of using the ^{208}Pb data.

For either case, the method of obtaining the background normalization factor $\alpha_{BG}(E_n)$, for scaling the background spectrum, $C_{BG}(E_n, E_{\text{Sum}})$, to the foreground + background spectrum, $C_{FG+BG}(E_n, E_{\text{Sum}})$, is described by Eq. (1).

$$\alpha_{BG}(E_n) = \frac{\int_{8.5 \text{ MeV}}^{10.5 \text{ MeV}} C_{FG+BG}(E_n, E_{\text{Sum}}) dE_{\text{Sum}}}{\int_{8.5 \text{ MeV}}^{10.5 \text{ MeV}} C_{BG}(E_n, E_{\text{Sum}}) dE_{\text{Sum}}} \quad (1)$$

III. NEUTRON FLUENCE CHARACTERIZATION

In the present analysis the ^6Li and ^{235}U beam monitors were used for neutron fluence determination and the ^3He monitor was used only for a consistency check. While ideally one would use a single beam monitor over the full range of E_n , resonances in the $^{235}\text{U}(n, f)$ cross section over the 1 eV to 1 keV range for the ^{235}U monitor and a strong resonance at ≈ 240 keV in the $^6\text{Li}(n, t)\alpha$ cross section for the ^6Li monitor limits the feasibility of using either one exclusively. The yield, i.e. number of recorded reactions at each energy, measured in the beam monitors, Y_{BM} , divided by the relevant reaction cross section, σ_{BM} , is directly proportional to the fluence of neutrons on the sample, $\Phi(E_n)$, as described by Eq. (2).

$$\Phi(E_n) = \kappa \frac{Y_{\text{BM}}(E_n)}{\sigma_{\text{BM}}(E_n)} \quad (2)$$

The yield of the ^6Li monitor divided by the $^6\text{Li}(n, t)\alpha$ cross section was normalized to the yield of the ^{235}U monitor divided by the $^{235}\text{U}(n, f)$ cross section over the range of 3 keV to 20 keV. Figure 2 shows the beam-monitor yields divided by the relevant beam-monitor re-

action cross sections acquired during the $^{65}\text{Cu}(n, \gamma)$ measurement. Below 3 keV all data is from the ^6Li monitor, between 3 and 20 keV the data is the average of the ^6Li and ^{235}U monitor, and above 20 keV the data is exclusively from the ^{235}U monitor.

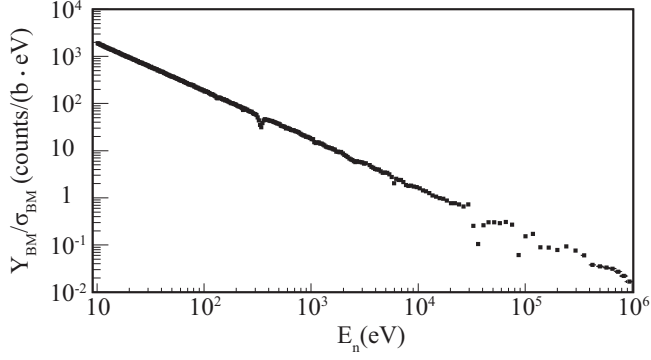


FIG. 2. Beam-monitor yields, Y_{BM} , divided by the relevant beam-monitor reaction cross sections, σ_{BM} , for the ^{65}Cu data. Below 3 keV all data is from the ^6Li monitor, between 3 and 20 keV the data is the average of the ^6Li and ^{235}U monitor, and above 20 keV the data is exclusively from the ^{235}U monitor.

The normalization of the beam-monitor response, κ from Eq. (2), was deduced from a measurement of $^{197}\text{Au}(n, \gamma)$ on the 4-mm diameter, 5 kÅ thick, ^{197}Au sample. Prior to the experiment, the thickness of the ^{197}Au sample was measured using Rutherford Backscattering, placing an uncertainty on the number of ^{197}Au atoms in the sample of 4%. The measured $^{197}\text{Au}(n, \gamma)$ yield, $Y_{\text{Au}}(E_n)$ is related to the $^{197}\text{Au}(n, \gamma)$ cross section, $\sigma_{\text{Au}}(E_n)$, by Eq. (3).

$$Y_{\text{Au}}(E_n) = \Phi(E_n) N_{\text{Au}} \sigma_{\text{Au}}(E_n) \quad (3)$$

Substituting Eq. (2) in for $\Phi(E_n)$ in Eq. (3) one obtains Eq. (4) relating the $^{197}\text{Au}(n, \gamma)$ yield to the beam-monitor yields allowing for extraction of the normalization factor κ .

$$Y_{\text{Au}}(E_n) = \kappa \frac{Y_{\text{BM}}(E_n)}{\sigma_{\text{BM}}(E_n)} N_{\text{Au}} \sigma_{\text{Au}}(E_n) \quad (4)$$

The normalization of the beam-monitor response was performed over the 4.89-eV resonance in the $^{197}\text{Au}(n, \gamma)$ cross section. All crystal multiplicities were used and no cuts were placed on E_{Sum} .

The foreground E_{Sum} shape for neutron capture on ^{197}Au , $F_{\text{Au}}(E_{\text{Sum}})$, was determined from the $^{197}\text{Au}(n, \gamma)$ data. Background E_{Sum} spectra were taken from symmetric regions in TOF closely surrounding the 4.89-eV resonance. In this case $C_{\text{FG+BG}}(E_n, E_{\text{Sum}})$ was obtained from the data encapsulated between these two background regions. The background spectra were summed to obtain $C_{\text{BG}}(E_n, E_{\text{Sum}})$ and subsequently normalized

to $C_{\text{FG+BG}}(E_n, E_{\text{Sum}})$ using Eq. (1). The scaled background, $\alpha_{\text{BG}}(E_n) C_{\text{BG}}(E_n, E_{\text{Sum}})$, was then subtracted from the $C_{\text{FG+BG}}(E_n, E_{\text{Sum}})$ to extract $F_{\text{Au}}(E_{\text{Sum}})$.

The background component described above taken nearby the 4.89-eV resonance contains too much of the $^{197}\text{Au}(n, \gamma)$ yield to serve as the background used for the extraction of the $^{197}\text{Au}(n, \gamma)$ yield. Therefore, a different background component, $C'_{\text{BG}}(E_n, E_{\text{Sum}})$, was determined in a similar manner as before from a linear combination of symmetric regions in TOF about the 4.89-eV resonance, but this time much further away from the resonance such that minimal ($< 1\%$) foreground is present. The E_{Sum} spectrum for each E_n bin from 4 to 6 eV, shown in Figure 3a, was then fit with a combination of the scaled $F_{\text{Au}}(E_{\text{Sum}})$ and $\alpha'_{\text{BG}}(E_n) C'_{\text{BG}}(E_n, E_{\text{Sum}})$. Figure 4 shows an example fit of a E_{Sum} spectrum from a single E_n bin, shown in black. The scaled $F_{\text{Au}}(E_{\text{Sum}})$ is shown in dotted blue, and scaled background component, $\alpha'_{\text{BG}}(E_n) C'_{\text{BG}}(E_n, E_{\text{Sum}})$, is shown in dashed red.

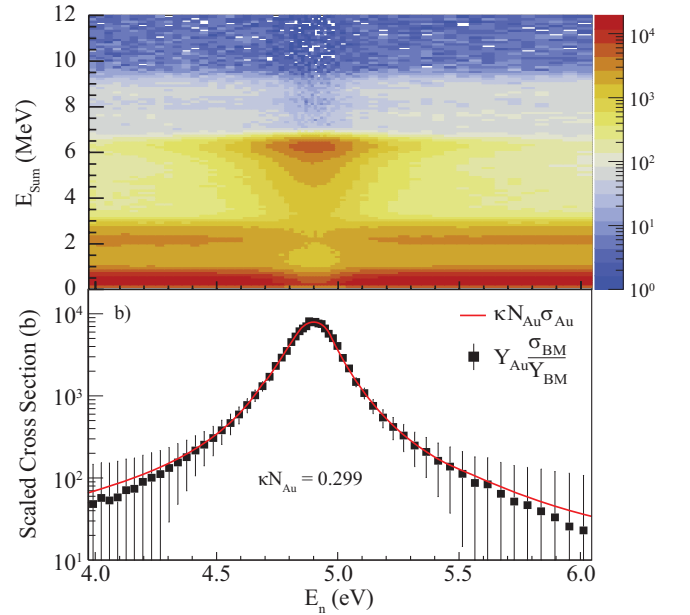


FIG. 3. a) E_{Sum} as a function of E_n for the $^{197}\text{Au}(n, \gamma)$ data. b) Extracted yield for each E_n bin in a) shown as black squares while a fit of the ENDF/B-VIII.0 $^{197}\text{Au}(n, \gamma)$ cross section, corrected for the response of the target-moderator assembly, to the data is shown in red.

The extracted yield as a function of E_n is represented by black squares in Figure 3b. A fit of the ENDF/B-VIII.0 $^{197}\text{Au}(n, \gamma)$ cross section, adjusted for the response of the spallation target-moderator assembly, to the extracted yield is shown in red. The scale factor for the ENDF cross section to the experimentally determined yield, κN_{Au} , is 0.299 atoms per barn. To evaluate the uncertainty of κN_{Au} a bootstrap technique was employed where fifty ^{197}Au runs were selected at random 100 times and κN_{Au} was determined for each block of runs using the analysis techniques described in this section. The

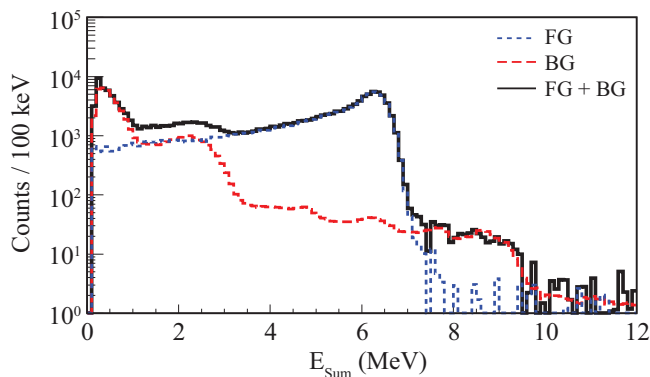


FIG. 4. (color online) Example fit of a single E_n bin along the x axis of Fig. 3a projected onto the y axis. The raw data from the projection, shown in black, is a combination of foreground neutron-capture, shown in dotted blue, and scattered-neutron background shown in dashed red.

distribution of κN_{Au} was fit with a Gaussian and a 1σ uncertainty of 3.5 % was determined. The impact on κN_{Au} from variations of the extracted foreground E_{Sum} shape due to choices of the E_n ranges selected for the various foreground and background regions was determined to be 5 %.

IV. DATA ANALYSIS AND RESULTS

The analysis of ^{65}Cu proceeds following the time and energy calibrations described in section II. The raw $^{65}\text{Cu}(n, \gamma)$ data is presented in Fig. 5. E_{Sum} is on the vertical axis while E_n is on the horizontal axis. The color scale on the third axis represents the number of counts for each E_{Sum} and E_n . Crystal multiplicities of 2 through 10 are considered for this analysis. The bulk of events with $M_{Cr} = 1$ are scattered-neutron capture events inside the BaF_2 crystals and above $M_{Cr} = 10$ there are very few events dominated by cosmic rays and pileup. A 150-keV threshold has been applied to all DANCE crystals.

The data presented in Fig. 5 contain several components that must be characterized to extract the $^{65}\text{Cu}(n, \gamma)$ cross section. The most valuable information for identifying these components in DANCE are neutron-capture Q-values and measured E_{Sum} values. The maximum possible E_{Sum} value, barring pileup, is the sum of the neutron-capture Q-value and E_n . When examining the data in Fig. 5 one can see several resonances in $^{65}\text{Cu}(n, \gamma)$ with E_{Sum} values peaking just below the 7.065-MeV Q-value. There is also evidence of neutron-capture on the predominant contaminant, ^{63}Cu . These events have E_{Sum} values peaking just below the 7.916-MeV $^{63}\text{Cu}(n, \gamma)$ Q-value, and are readily observed around $E_n \approx 580$ eV, the energy of the strongest $^{63}\text{Cu}(n, \gamma)$ resonance. There are strong horizontal bands around E_{Sum} of 4.7 MeV and 9.1 MeV from the capture of thermalized, scattered neutrons on ^{138}Ba and ^{135}Ba , respectively.

Contributions from the other stable Ba isotopes are also present.

A. Deadtime and Pileup Corrections

When a crystal of DANCE triggers a channel in the data acquisition system, the charge integral of the triggered channel is recorded for 1 μs . The instantaneous event rate at short TOF as well as on some resonances is often high with respect to the relatively long 1 μs charge integration window. During the charge integration period a channel cannot retrigger, but the charge integral will include a fraction of any subsequent radiation that hit that crystal within 1 μs of the first event. This is referred to as crystal pileup and results in an increase in the measured crystal energy of one or more crystals, and thus E_{Sum} , of the first event. This also gives rise to the deadtime in DANCE. Since a crystal recording charge hit with subsequent radiation is unable to trigger, the observed M_{Cr} as well as the recorded E_{Sum} of the second event is reduced. A smaller effect from recording two events within the 5-ns event-building window is also observed and is referred to as event pileup. Event- and crystal-pileup effects manifest themselves in Fig. 5 as vertical bands on strong resonances that extend in E_{Sum} beyond the neutron-capture Q-value.

The characterization of these effects and methods to correct the data for them is beyond the scope of this paper, and are described in detail in Ref. [11]. The basic concept behind these methods is to use the measured event rates for all recorded multiplicities, the average number of crystals recording charge integrals at any given time, and the known event and charge integration lengths to deduce the probability of event pileup, deadtime, and crystal pileup occurring, as well as their impacts on the recorded data. Those methods applied to the present data yield excellent results over the entire energy range relevant for calculating the Maxwellian Averaged Cross Section (MACS) of ^{65}Cu . A slight deficiency in the crystal pileup technique for the first resonance in both the $^{63,65}\text{Cu}$ data, where instantaneous count rates vary by an order of magnitude, is still being investigated, but affects the extracted MACS at a less than 0.2 % level for all energies reported in this manuscript.

B. Contaminant Characterization

The small amount of ^{63}Cu (0.3 %), is clearly visible in Fig. 5, and thus its contribution must be subtracted. Data collected on the ^{63}Cu , ^{65}Cu , and ^{208}Pb samples in the region around $E_n = 580$ eV, the location of the strongest resonance is $^{63}\text{Cu}(n, \gamma)$, was used. The scattered-neutron background was approximated by the ^{208}Pb data scaled using Eq. (1) and subtracted from the ^{63}Cu and ^{65}Cu data. Then, the ratio of the integral of counts ($^{65}\text{Cu}/^{63}\text{Cu}$) in the region between 7.5 and 8.5

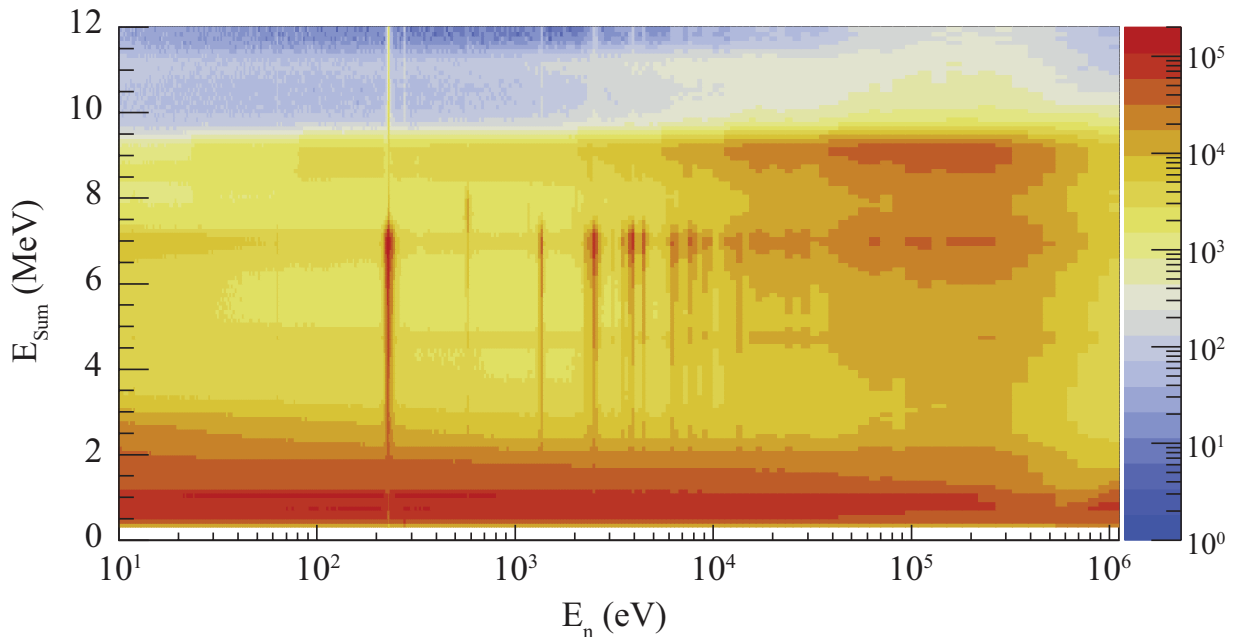


FIG. 5. (color online) Counts as a function of E_{Sum} and E_n for the $^{65}\text{Cu}(n, \gamma)$ data.

MeV in E_{Sum} , which brackets the 7.916-MeV $^{63}\text{Cu}(n, \gamma)$ Q-value, is above the 7.065-MeV $^{65}\text{Cu}(n, \gamma)$ Q-value, and is below the 9.108-MeV $^{135}\text{Ba}(n, \gamma)$ Q-value, is the scaling factor for the ^{63}Cu data. The ^{63}Cu data was scaled and subtracted from the ^{65}Cu data to remove the contribution of $^{63}\text{Cu}(n, \gamma)$ across all E_n simultaneously. The $^{63}\text{Cu}(n, \gamma)$ subtracted $^{65}\text{Cu}(n, \gamma)$ data corrected for event pileup, deadtime, and crystal pileup is shown in Fig. 6.

Smaller contributions from unknown contaminants at ≈ 60 eV and ≈ 1.2 keV are also present, but have a negligible effect on the MACS values presented herein.

C. Energy-Differential Cross Section

For each E_n bin of the $^{65}\text{Cu}(n, \gamma)$ data in Fig. 6 a background component, $C_{208\text{Pb}}(E_n, E_{\text{Sum}})$, was taken from the ^{208}Pb data, and a scaling factor, $\alpha_{208\text{Pb}}(E_n)$, was determined using Eq. (1). Figure 7 presents a sample fit where the ^{65}Cu data is shown in black and the scattered-neutron background, obtained from the ^{208}Pb

data and scaled using Eq. (1), is shown in dashed red. The $^{65}\text{Cu}(n, \gamma)$ yield, $Y_{65\text{Cu}}(E_n)$, was determined using Eq. (5)

The $^{65}\text{Cu}(n, \gamma)$ yield was then converted to the $^{65}\text{Cu}(n, \gamma)$ cross section using Eq. (6), where κ is the cross-section normalization factor determined in section III and $\epsilon_{65\text{Cu}}$ is the DANCE cascade efficiency for $^{65}\text{Cu}(n, \gamma)$.

The value of $\epsilon_{65\text{Cu}}$ was determined from DICEBOX [12] coupled with GEANT4 [13] simulations. Prior to this effort the GEANT4 model of DANCE [14] was validated using a variety of radioactive check sources. Simultaneous agreement between experimental and simulated crystal multiplicities, crystal energies, and total efficiencies better than 0.5% absolute for all sources was achieved.

DICEBOX simulations were performed for all possible spins and parities, J^π , of capture states for both s-wave and p-wave neutron capture. A backshifted Fermi gas model was chosen for the level density with a spin cut off parameter from Ref. [15] and level density parameters from Ref. [16]. A standard Lorentzian shape was chosen for the E1 photon strength function with parameters taken from Ref. [17].

$$Y_{65\text{Cu}}(E_n) = \int_{5.5 \text{ MeV}}^{7.5 \text{ MeV}} [C_{65\text{Cu}}(E_n, E_{\text{Sum}}) - \alpha_{208\text{Pb}}(E_n)C_{208\text{Pb}}(E_n, E_{\text{Sum}})] dE_{\text{Sum}} \quad (5)$$

DICEBOX was used to generate 800 simulations, each with 100000 capture events, for each possible J^π from s-

and p-wave neutron capture. The γ -ray cascades from these capture events were then processed through the

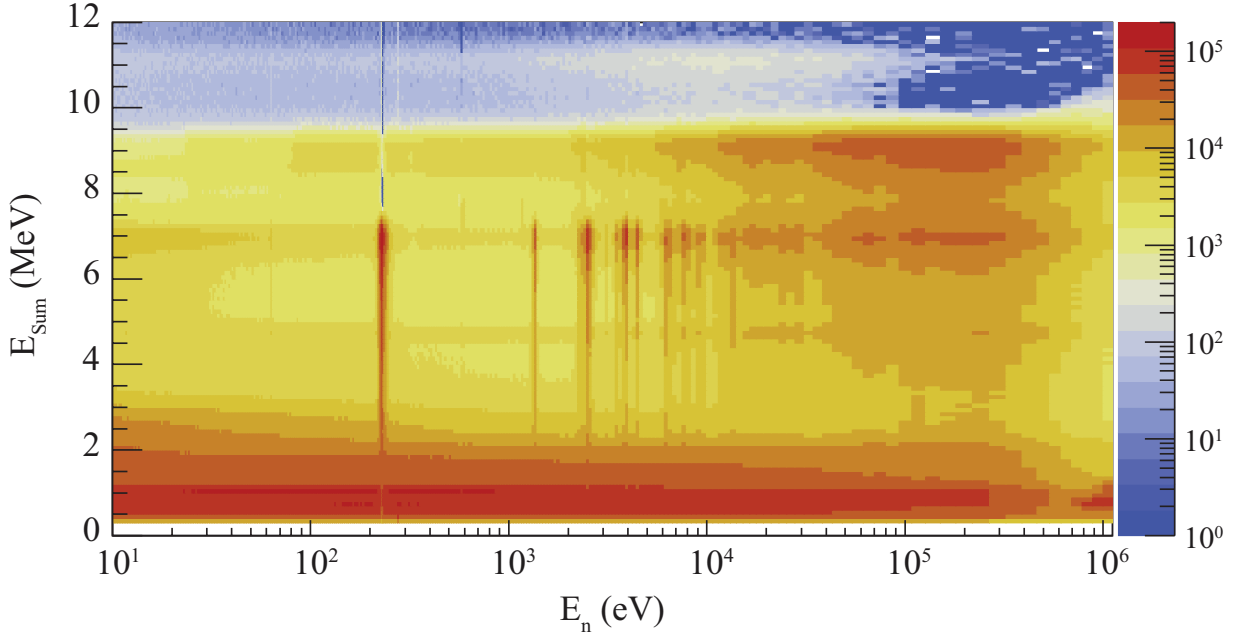


FIG. 6. (color online) Counts as a function of E_{Sum} and E_n for the $^{65}\text{Cu}(n, \gamma)$ data following the corrections for event pileup, deadtime, and crystal pileup. The contribution from $^{63}\text{Cu}(n, \gamma)$ from the ^{63}Cu contaminant has also been subtracted.

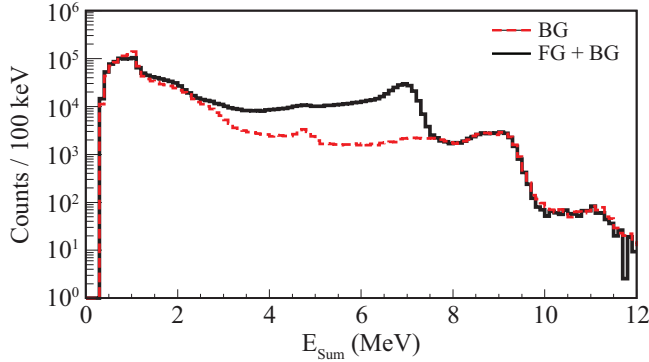


FIG. 7. (color online) Demonstration of background characterization for a single E_n bin of the ^{65}Cu data. The ^{65}Cu data is shown in black, and the scattered-neutron background, obtained from the ^{208}Pb data and scaled using Eq. (1), is shown in dashed red.

GEANT4 model of DANCE. The resulting γ -ray energy and multiplicity spectra from these simulations were compared with the experimental data to verify agreement at a level reasonable for estimating the cascade detection efficiency. The same 150-keV E_{Cr} threshold and $2 \leq M_{Cr} \leq 10 M_{Cr}$ cuts applied to the data were applied to the simulation. The wide range of M_{Cr} accepted in the analysis made it possible to find an E_{Sum} range, 5.5 MeV to 7.5 MeV in this case, where all extracted cascade efficiency values were within 5% percent of one another. Table 1 presents a summary of $\epsilon_{65\text{Cu}}$ values obtained from these simulations. The average value

of 0.45 ± 0.02 was used for $\epsilon_{65\text{Cu}}$ in the analysis.

TABLE I. Values of $\epsilon_{65\text{Cu}}$ obtained from DICEBOX cascades propagated through the DANCE GEANT4 model for s-wave and p-wave neutron capture. The ground state spin and parity of ^{65}Cu is $3/2^-$.

Capture State J^π	$\epsilon_{65\text{Cu}}$
3^+	0.441 ± 0.008
2^+	0.440 ± 0.006
1^+	0.441 ± 0.007
0^+	0.442 ± 0.010
2^-	0.482 ± 0.013
1^-	0.474 ± 0.015
Average	0.453 ± 0.020

$$\sigma_{65\text{Cu}}(E_n) = \frac{Y_{65\text{Cu}}(E_n)}{\epsilon_{65\text{Cu}} \kappa N_{65\text{Cu}}} \frac{\sigma_{\text{BM}}(E_n)}{Y_{\text{BM}}(E_n)} \quad (6)$$

The extracted $^{65}\text{Cu}(n, \gamma)$ energy-differential cross section shown as black squares in Fig. 8. A change between ENDF/B-VII.1 and ENDF/B-VIII.0 introduced a resonance at $E_n \approx 580$ eV that is not supported by the present measurement. However, since this energy corresponds to the location of the largest resonance in ^{63}Cu it suggests the possibility that results influencing the updated evaluation could be affected by ^{63}Cu contamination.

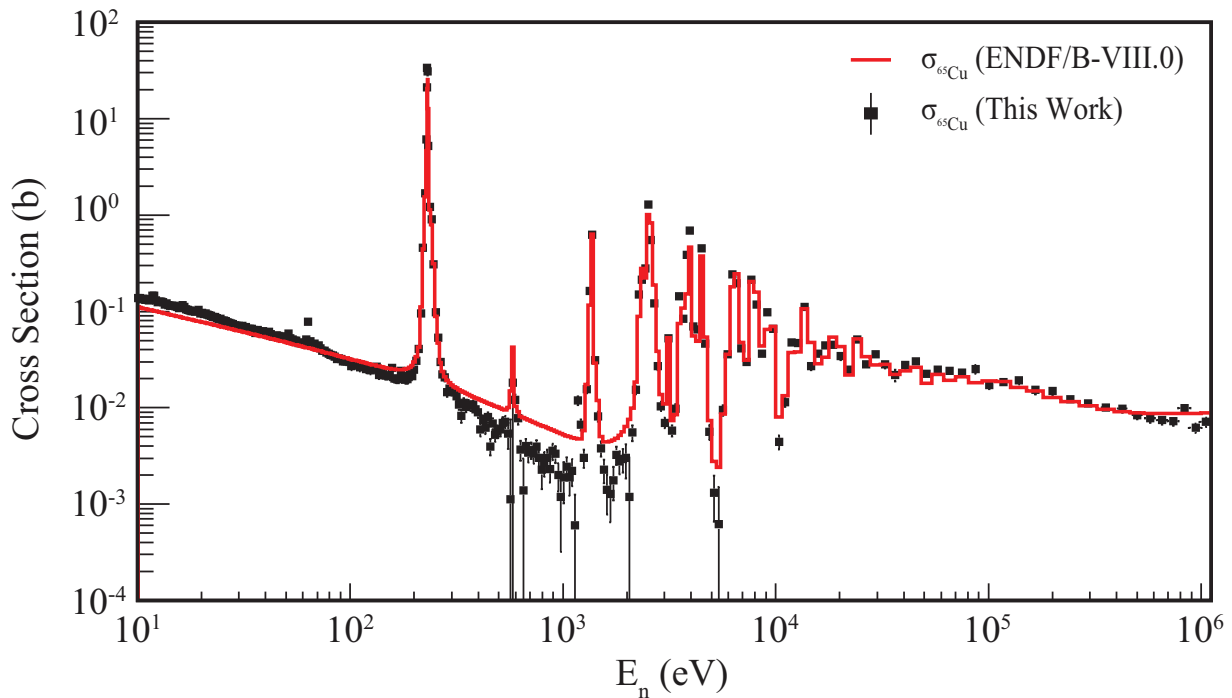


FIG. 8. (color online) Energy differential $^{65}\text{Cu}(n, \gamma)$ cross section shown in black squares. The ENDF/B-VIII.0 $^{65}\text{Cu}(n, \gamma)$ cross section, corrected for the response of the target-moderator assembly, is shown in red.

D. Uncertainties

There are several statistical and systematic uncertainties that must be accounted for in the analysis.

DANCE relies on the neutron TOF to deduce E_n , and thus any uncertainty in TOF must be propagated as uncertainty in E_n . There are three primary sources of TOF uncertainty. At high E_n , the largest of these is the pulse width of the proton beam responsible for producing spallation neutrons. The time profile of the beam is nominally triangular with a FWHM of 120 ns. The second source of TOF uncertainty is the moderation time distribution of neutrons and is E_n dependent. The last TOF uncertainty comes from the response of DANCE itself. For all γ -ray energies of interest the coincidence resolving time is better than 1.5 ns.

The DANCE capture data for all measured samples for every E_n bin has an associated statistical error. The uncertainty from subtraction of the ^{63}Cu contaminant and the scattered-neutron background from the ^{65}Cu data was propagated into the differential cross section for each E_n bin.

Like the DANCE capture data, beam-monitor yields also have a statistical error for each E_n bin and there is an uncertainty in the relevant reaction cross sections used to obtain $Y_{\text{BM}}/\sigma_{\text{BM}}$. There is also an uncertainty from the normalization of $Y_{6\text{Li}}/\sigma_{6\text{Li}}$ to $Y_{235\text{U}}/\sigma_{235\text{U}}$. These uncertainties were also propagated to the differential cross section.

In addition to the uncertainties mentioned above there

are a variety of systematic uncertainties provided in Table 2. Items in Table 2 with normal-faced text originate from the neutron fluence normalization and were added in quadrature to obtain the "Neutron fluence Normalization" uncertainty. Items in Table 2 with bold-faced text were added in quadrature to obtain the final systematic uncertainty.

TABLE II. Systematic uncertainties in the analysis. Quantities in normal-faced text are from the neutron fluence normalization and were added in quadrature to obtain the "Neutron Fluence Normalization" uncertainty. Items in bold-faced text were added in quadrature to obtain the final systematic uncertainty.

Uncertainty Component	1σ Uncertainty (%)
Number of ^{197}Au Atoms	4.0
Foreground ^{197}Au E_{Sum} Shape	5.0
Extraction of κN_{Au}	3.5
^{197}Au Cross Section	2.7
Neutron Fluence Normalization	7.8
Number of ^{65}Cu Sample Atoms	0.2
DANCE ^{65}Cu Cascade Efficiency	4.4
TOTAL	8.9

E. Maxwellian-Averaged Cross Section

The measured differential cross section shown in Fig. 8 was converted to a Maxwellian-Averaged Cross Section

(MACS) using equation Eq. (7) where μ is the reduced mass and $\delta(E_n)$ is the bin width of the bin centered on E_n .

$$\sigma^{\text{MACS}}(kT) = \frac{2}{\sqrt{\pi}} \left(\frac{\mu}{kT} \right)^2 \sum_{E_n=10 \text{ eV}}^{1 \text{ MeV}} \sigma(E_n) E_n e^{\frac{E_n}{kT}} \delta(E_n) \quad (7)$$

The resulting MACS for $^{65}\text{Cu}(n, \gamma)$ for energies between 5 and 100 keV are presented in Table II. The E_n range of 10 eV to 1 MeV in for the summation in Eq. (7) results in $> 99.8\%$ of the Maxwell-Boltzmann distribution included in the calculation of the MACS, across all kT , and thus any associated uncertainty from truncation of the E_n range is negligible.

TABLE III. Comparison of Maxwellian Averaged Cross Sections determined in the present work with KADoNiS v0.3.

$k_B T$ (keV)	MACS (mb)	MACS (mb)
	KADoNiS v0.3	This Work
5	111	$132.6 \pm 0.6_{\text{stat}} \pm 12_{\text{sys}}$
10	57.5	$78.9 \pm 0.4_{\text{stat}} \pm 7.0_{\text{sys}}$
15	42.2	$58.2 \pm 0.4_{\text{stat}} \pm 5.2_{\text{sys}}$
20	35.6	$47.7 \pm 0.4_{\text{stat}} \pm 4.2_{\text{sys}}$
25	32.0	$41.3 \pm 0.4_{\text{stat}} \pm 3.7_{\text{sys}}$
30	29.8 ± 1.3	$37.0 \pm 0.3_{\text{stat}} \pm 3.3_{\text{sys}}$
40	26.9	$31.5 \pm 0.3_{\text{stat}} \pm 2.8_{\text{sys}}$
50	24.0	$28.0 \pm 0.3_{\text{stat}} \pm 2.5_{\text{sys}}$
60	22.5	$25.6 \pm 0.3_{\text{stat}} \pm 2.3_{\text{sys}}$
80	19.6	$22.0 \pm 0.3_{\text{stat}} \pm 2.0_{\text{sys}}$
100	18.2	$19.7 \pm 0.2_{\text{stat}} \pm 1.7_{\text{sys}}$

V. ASTROPHYSICAL IMPACT

Recent experiments have improved our knowledge of the (n, γ) cross sections for ^{63}Ni [2], ^{63}Cu [1] and ^{65}Cu (this work), all of which impact the abundances of $^{63,65}\text{Cu}$. The full impact of updates to these (n, γ) cross sections were investigated for the complete nucleosynthesis of 15, 20 and 25 M_\odot massive star models from [18] and [19] computed using the KEPLER code [20–22]. The method for the nucleosynthesis calculations was the following. Stellar evolution models were evolved from the main sequence through to the pre-supernova stage. The temperature, density and diffusion coefficient¹ from stellar evolution models were saved every computational time step. We then used the NuGrid post-processing code MPPNP [19, 23, 24], which solves the reaction equations on each grid cell and subsequently performs a diffusion solve in operator split on the whole domain for the mixing. This process was repeated every time step.

¹ Mixing processes including convection and semiconvection in the stellar models were modelled as a diffusive process.

The reaction network used for the post-processing consisted of 1092 isotopes and approximately 14000 reactions. A detailed description of where we take the reaction rates from can be found in [19, 25, 26, and references therein]. The time integration was performed using a fully implicit backward-Euler method with a Newton-Raphson scheme. At temperatures above 6 GK the nuclear statistical equilibrium (NSE) approximation was used to solve for the composition, which assumes that the strong reaction rates are in equilibrium. The weak reaction rates are then coupled to the NSE state using a 4th/5th order Runge-Kutta type Cash-Karp time integrator [27].

The final composition of the models at the presupernova stage is shown in Figure 9, where we have allowed the unstable isotopes to decay for 10^{16} s. The left panels show the composition relative to the Solar abundance distribution and the right panels show the relative difference when the three updated (n, γ) cross sections are used. We only consider the composition of the portion of the star that will be ejected in the supernova explosion, i.e. we neglect the innermost region of the core that will become the compact remnant (neutron star or black hole). We have also neglected the impact of any shock heating during the supernova explosion on the composition. This tends to destroy the s-process products in the carbon shell. Some s-process isotopes such as ^{60}Fe can also be produced in the carbon and helium shells during the explosion, but our tests indicate that the majority of the isotopes in Figure 9 are not significantly produced in the carbon or helium shells during the explosion.

Figure 9 shows that there is approximately 20 per cent less ^{63}Cu and 10 percent less ^{65}Cu produced when the new cross sections are adopted, and an overall increase in the weak s-process elements from Zn to Zr up to 20 percent, peaking around Kr.

VI. CONCLUSION

The $^{65}\text{Cu}(n, \gamma)$ cross section was measured with DANCE located at LANSCE of LANL. MACS values extracted from the data are significantly higher than the most recent measurements [5] but are in agreement with those extracted from prior measurements [4]. The impact of this new $^{65}\text{Cu}(n, \gamma)$ cross section coupled with updated $^{63}\text{Cu}(n, \gamma)$ [1] and $^{63}\text{Ni}(n, \gamma)$ [2] cross sections were investigated for the complete nucleosynthesis of 15, 20 and 25 M_\odot massive star models from [18] and [19] computed using the KEPLER code [20–22]. Decrease in abundances for $^{63,65}\text{Cu}$ by 20 and 10 percent, respectively, were observed along with an overall increase of 20 percent in nucleosynthesis yield of elements from Zn to Zr. In particular these new results enhance the production of s-only isotopes ^{70}Ge , ^{76}Se , and $^{80,82}\text{Kr}$. This impacts the s-process nucleosynthesis calibration for the weak component as well as abundances that must be accounted for by proposed LEPP [28] or other novel nu-

cleosynthesis mechanisms.

ACKNOWLEDGMENTS

This work benefited from the use of the LANSCE accelerator facility. Work was performed under the auspices of the US Department of Energy through the Los Alamos National Laboratory. Los Alamos National Laboratory is operated by Triad National Security, LLC, for the National Nuclear Security Administration of U.S. Department of Energy (Contract No. 89233218CNA000001). This research used resources provided by the Los Alamos National Laboratory Institutional Computing Program, which is supported by the U.S. Department of Energy National Nuclear Security Administration also under Contract No. 89233218CNA000001. Research presented in this manuscript was supported by the Laboratory Directed Research and Development program of Los Alamos National Laboratory under project numbers LDRD-20160173ER and LDRD-20170687PRD3. The project was also supported by the Czech Science Foundation under Grant No. 19-14048S. The ^{65}Cu isotopes used in this research were supplied by the United States Department of Energy Office of Science by the Isotope Program in the Office of Nuclear Physics.

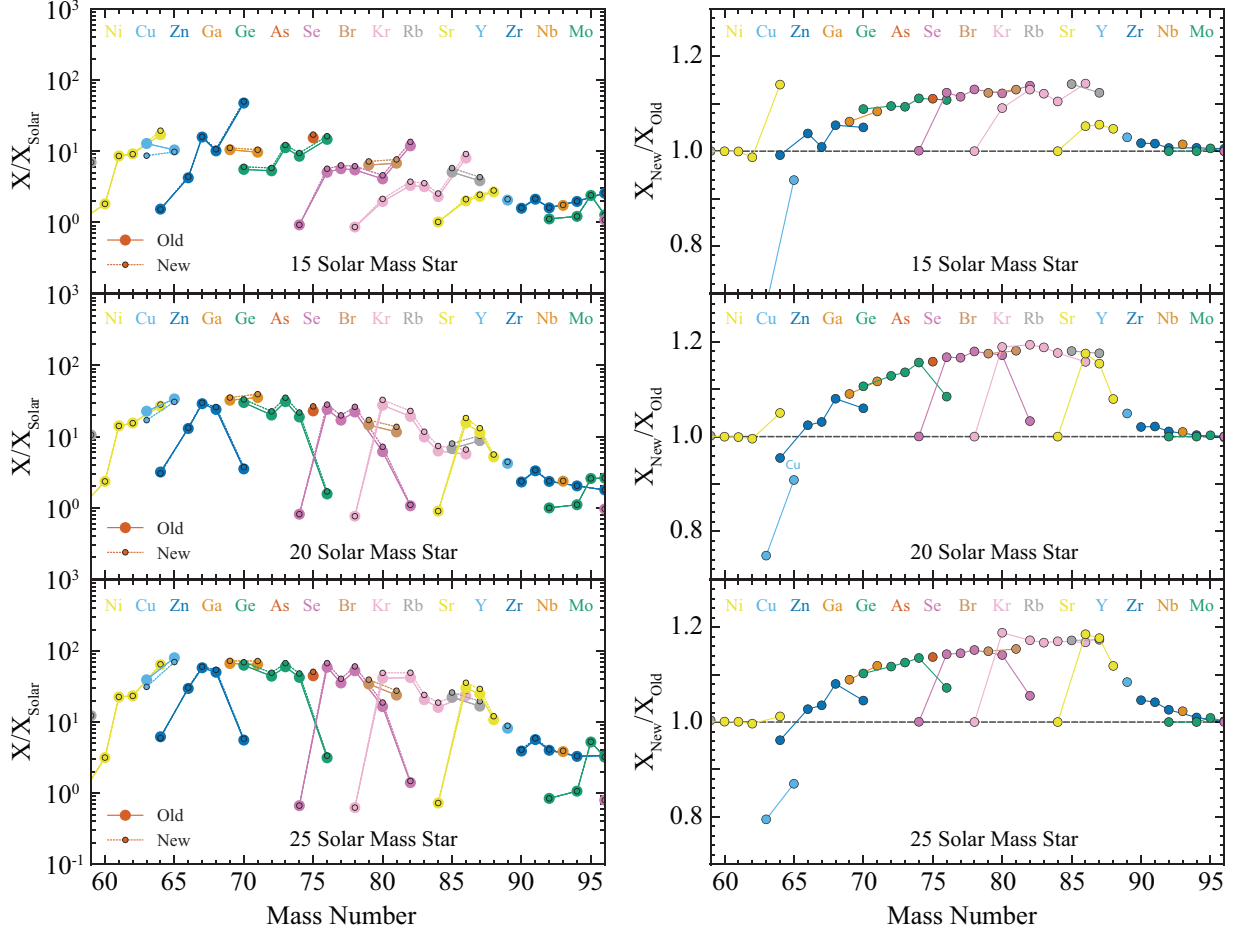


FIG. 9. (color online) The final composition of the models at the presupernova stage for 15, 20 and 25 M_{\odot} massive star models from [18] and [19] computed using the KEPLER code [20–22]. Unstable isotopes to have been allowed to decay for 10^{16} s. The left panels show the composition relative to the Solar abundance distribution while the right panels show the relative difference when the three updated (n, γ) cross sections are used.

REFERENCES

-
- [1] M. Weigand, C. Beinrucker, A. Couture, S. Fiebiger, M. Fonseca, K. Göbel, M. Heftrich, T. Heftrich, M. Jandel, F. Käppeler, A. Krása, C. Lederer, H. Y. Lee, R. Plag, A. Plompen, R. Reifarh, S. Schmidt, K. Sonnabend, and J. L. Ullmann, *Phys. Rev. C* **95**, 015808 (2017).
- [2] M. Weigand, T. A. Bredeweg, A. Couture, K. Göbel, T. Heftrich, M. Jandel, F. Käppeler, C. Lederer, N. Kivel, G. Korschinek, M. Krtička, J. M. O'Donnell, J. Ostermüller, R. Plag, R. Reifarh, D. Schumann, J. L. Ullmann, and A. Wallner, *Phys. Rev. C* **92**, 045810 (2015), arXiv:1512.02263 [nucl-ex].
- [3] F. Käppeler, R. Gallino, S. Bisterzo, and W. Aoki, *Rev. Mod. Phys.* **83**, 157 (2011).
- [4] M. S. Pandey, J. B. Garg, and J. A. Harvey, *Phys. Rev. C* **15**, 600 (1977).
- [5] M. Heil, F. Käppeler, E. Uberseder, R. Gallino, and M. Pignatari, *Phys. Rev. C* **77**, 015808 (2008).
- [6] M. Heil, R. Reifarh, M. Fowler, R. Haight, F. Käppeler, R. Rundberg, E. Seabury, J. Ullmann, J. Wilhelmy, and K. Wisshak, *Nuclear Instruments and Methods in Physics Research Section A: Accelerators, Spectrometers, Detectors and Associated Equipment* **459**, 229 (2001).
- [7] P. W. Lisowski, C. D. Bowman, G. J. Russell, and S. A. Wender, *Nuclear Science and Engineering* **106**, 208 (1990), <https://doi.org/10.13182/NSE90-A27471>.
- [8] M. Mocko and G. Muhrer, *Nuclear Instruments and Methods in Physics Research Section A: Accelerators, Spectrometers, Detectors and Associated Equipment* **704**, 27 (2013).
- [9] S. Mobsy, A. J. Couture, M. Jandel, and J. M. O'Donnell, "Data acquisition upgrade for DANCE," LA-UR-18-22130 (2018).
- [10] L. Zavorka, M. J. Mocko, and P. E. Koehler, *Nuclear Instruments and Methods in Physics Research Section A: Accelerators, Spectrometers, Detectors and Associated Equipment* **901**, 189 (2018).
- [11] C. J. Prokop, A. Couture, and S. Mosby, *Nuclear Instruments and Methods in Physics Research Section A: Accelerators, Spectrometers, Detectors and Associated Equipment* (In Preparation) (2018).
- [12] F. Bečvář, *Nuclear Instruments and Methods in Physics Research Section A: Accelerators, Spectrometers, Detectors and Associated Equipment* **417**, 434 (1998).
- [13] S. Agostinelli, J. Allison, K. Amako, J. Apostolakis, H. Araujo, P. Arce, M. Asai, D. Axen, S. Banerjee, G. Barrand, F. Behner, L. Bellagamba, J. Boudreau, L. Broglia, A. Brunengo, H. Burkhardt, S. Chauvie, J. Chuma, R. Chytráček, G. Cooperman, G. Cosmo, P. Degtyarenko, A. Dell'Acqua, G. Depaola, D. Dietrich, R. Enami, A. Feliciello, C. Ferguson, H. Fesefeldt, G. Folger, F. Foppiano, A. Forti, S. Garelli, S. Giani, R. Giannitrapani, D. Gibin, J. G. Cadenas, I. González, G. G. Abril, G. Greeniaus, W. Greiner, V. Grichine, A. Grossheim, S. Guatelli, P. Gumplinger, R. Hamatsu, K. Hashimoto, H. Hasui, A. Heikkinen, A. Howard, V. Ivanchenko, A. Johnson, F. Jones, J. Kallenbach, N. Kanaya, M. Kawabata, Y. Kawabata, M. Kawaguti, S. Kelner, P. Kent, A. Kimura, T. Kodama, R. Kokoulin, M. Kossov, H. Kurashige, E. Lamanna, T. Lampén, V. Lara, V. Lefebvre, F. Lei, M. Liendl, W. Lockman, F. Longo, S. Magni, M. Maire, E. Medernach, K. Minamimoto, P. M. de Freitas, Y. Morita, K. Murakami, M. Nagamatsu, R. Nartallo, P. Nieminen, T. Nishimura, K. Ohtsubo, M. Okamura, S. O'Neale, Y. Oohata, K. Paech, J. Perl, A. Pfeiffer, M. Pia, F. Ranjard, A. Rybin, S. Sadilov, E. D. Salvo, G. Santin, T. Sasaki, N. Savvas, Y. Sawada, S. Scherer, S. Sei, V. Sirotenko, D. Smith, N. Starkov, H. Stoecker, J. Sulkimo, M. Takahata, S. Tanaka, E. Tcherniaev, E. S. Tehrani, M. Tropeano, P. Truscott, H. Uno, L. Urban, P. Urban, M. Verderi, A. Walkden, W. Wander, H. Weber, J. Wellisch, T. Wenaus, D. Williams, D. Wright, T. Yamada, H. Yoshida, and D. Zschesche, *Nuclear Instruments and Methods in Physics Research Section A: Accelerators, Spectrometers, Detectors and Associated Equipment* **506**, 250 (2003).
- [14] M. Jandel, T. Bredeweg, A. Couture, M. Fowler, E. Bond, M. Chadwick, R. Clement, E.-I. Esch, J. O'Donnell, R. Reifarh, R. Rundberg, J. Ullmann, D. Vieira, J. Wilhelmy, J. Wouters, R. Macri, C. Wu, and J. Becker, *Nuclear Instruments and Methods in Physics Research Section B: Beam Interactions with Materials and Atoms* **261**, 1117 (2007), the Application of Accelerators in Research and Industry.
- [15] D. Bucurescu and T. v. Egidy, *Phys. Rev. C* **72**, 067304 (2005).
- [16] T. v. Egidy and D. Bucurescu, *Phys. Rev. C* **72**, 044311 (2005).
- [17] S. S. Dietrich and B. L. Berman, *Atomic Data and Nuclear Data Tables* **38**, 199 (1988).
- [18] C. L. Fryer, S. Andrews, W. Even, A. Heger, and S. Safi-Harb, *Astrophys. J.* **856**, 63 (2018), arXiv:1712.03415 [astro-ph.HE].
- [19] S. Jones, H. Möller, C. Fryer, C. Fontes, R. Trappitsch, W. Even, A. Couture, M. Mumpower, and S. Safi-Harb, *MNRAS*, in preparation (2019).
- [20] T. A. Weaver, G. B. Zimmerman, and S. E. Woosley, *Astrophys. J.* **225**, 1021 (1978).
- [21] T. Rauscher, A. Heger, R. D. Hoffman, and S. E. Woosley, *Astrophys. J.* **576**, 323 (2002), astro-ph/0112478.
- [22] S. E. Woosley and A. Heger, *Phys. Rep.* **442**, 269 (2007), astro-ph/0702176.
- [23] M. Pignatari, F. Herwig, R. Hirschi, M. Bennett, G. Rockefeller, C. Fryer, F. X. Timmes, C. Ritter, A. Heger, S. Jones, U. Battino, A. Dotter, R. Trappitsch, S. Diehl, U. Frischknecht, A. Hungerford, G. Magkotsios, C. Travaglio, and P. Young, *ApJS* **225**, 24 (2016), arXiv:1307.6961 [astro-ph.SR].
- [24] C. Ritter, R. Androssy, B. Côté, F. Herwig, P. R. Woodward, M. Pignatari, and S. Jones, *MNRAS* **474**, L1 (2018), arXiv:1704.05985 [astro-ph.SR].
- [25] P. Denissenkov, G. Perdikakis, F. Herwig, H. Schatz, C. Ritter, M. Pignatari, S. Jones, S. Nikas, and A. Spy-

- rou, *Journal of Physics G Nuclear Physics* **45**, 055203 (2018).
- [26] S. Jones, F. Röpke, C. Fryer, A. Ruiter, I. Seitenzahl, L. Nittler, S. Ohlmann, R. Reifarth, M. Pignatari, and K. Belczynski, submitted to *A&A* (2019).
- [27] J. R. Cash and A. H. Karp, *ACM Trans. Math. Softw.* **16**, 201 (1990).
- [28] S. Cristallo, C. Abia, O. Straniero, and L. Pier-santi, *Astrophys. J.* **801**, 53 (2015), arXiv:1501.00544 [astro-ph.SR].